Using field measurements across land cover types to evaluate albedo-based wind friction velocity and estimate sediment transport

Zhuoli ZHOU[1], Chunlai ZHANG[1*], Adrian CHAPPELL[2], Xueyong ZOU[1], Zhuodong ZHANG[1], Xiaofeng ZUO[1], Xiaoyu ZHANG[1], Junxiong ZHOU[3], and Zihao CAO[4]

[1]State Key Laboratory of Earth Surface Processes and Resource Ecology, MOE Engineering Research Center of Desertification and Blown-sand Control, Faculty of Geographical Science, Beijing Normal University, Beijing 100875, China

[2]School of Earth and Environmental Sciences, Cardiff University, Cardiff CF10 3XQ, UK.

[3]Department of Bioproducts and Biosystems Engineering, University of Minnesota Twin Cities, St. Paul, MN 55108, USA.

[4]College of Surveying and Geo-Informatics, North China University of Water Resources and Electric Power, Zhengzhou 450046, China.

*Corresponding author: Chunlai Zhang (clzhang@bnu.edu.cn)

Key Points:

- Our estimates covered surfaces with a wide range of roughness configurations.
- We found extended evidence for scale invariance of albedo-based friction velocity.
- Albedo-based sediment transport accounted for the wind–roughness interaction.

Abstract

The soil surface wind friction velocity (u_{s*}) is an essential parameter for predicting sediment transport on rough surfaces. However, this parameter is difficult and time-consuming to obtain over large areas due to its spatiotemporal heterogeneity. The albedo-based approach calibrates laboratory measurements of aerodynamic properties with normalized shadow retrieved from any source of albedo data. This enables direct and cross-scale u_{s*} retrieval, but hasn't been evaluated against field measurements for different cover types. We evaluated the approach's performance using field friction velocity (u_*) measurements from ultrasonic anemometers. We retrieved coincident field pyranometer and satellite albedo across a wide range of land cover types including grassland, artificial shrubland, open shrubland and gobi cover types across the Inner Mongolia Plateau. For all cover types, u_* estimated from ultrasonic anemometers was close to the albedo-based results approach. Our results confirm and extend the findings that the approach works across scales from lab to field measurements, and permits large-area assessments using satellite albedo. We compared the seasonal sediment transport across the region calculated from albedo-based u_{s*} with results from an exemplar traditional transport model driven by u_* with aerodynamic roughness length varying with land cover type and fixed over time. The traditional model couldn't account for spatiotemporal variation in roughness elements and considerably over-estimated sediment transport, particularly in partially vegetated and gravel-covered central and western parts of the Inner Mongolia Plateau. The albedo-based sediment transport estimates will enable dynamic monitoring of the interaction between wind and surface roughness to support Earth System models.

Plain Language Summary

Reliable estimates of wind friction velocities at the soil surface are essential for accurately predicting sediment transport. We evaluated albedo-based wind friction velocity using ultrasonic anemometer and pyranometer field measurements on the Inner Mongolia Plateau. Measurements were made at 48 sites across a wide range of roughness from a variety of plant species with different densities, sizes and configurations and bare surfaces with differing amounts of gravel at the soil surface. Across the different land cover types, total wind friction velocity estimates from ultrasonic anemometers were almost the same, with very small bias, compared to the albedo-based approach. By conducting field measurements at multiple investigation sites, our findings demonstrate the performance of albedo models across different land surfaces and scales. The findings provide support for the parameterization of sediment transport and dust emission models.

Keywords: Wind friction velocity; aerodynamic sheltering; seasonal variation; sediment transport; albedo

1 Introduction

Soil erosion by wind has led to severe land degradation in arid and semi-arid areas, threatening the sustainable development of agriculture (Lal, 2003). The fine particle fraction at the soil surface, which typically contains the nutrient-rich and water-holding fraction that is important for soil health, is removed during sediment transport (Sterk et al., 1996). This fine fraction provides the main source of tropospheric aerosols (Pi and Sharratt, 2017) and transport of these materials reduces air quality and influences radiative forcing in the atmosphere, which affects global climate change (Darmenova et al., 2009; Kok et al., 2023). Wind is a critical factor for sediment transport and dust emission (Bergametti et al., 2020). In landscapes across Earth prone to sediment transport, the land surfaces are covered with a "canopy" of roughness elements such as vegetation and gravel, which reduce the wind speed acting on the soil surface and thus influence the intensity and spatial distribution of wind erosion (Zou et al., 2022). To best describe the wind erosion process, most aeolian transport models include the wind friction velocity (u_*) as an important parameter (Bagnold, 1941; Marticorena and Bergametti, 1995; Shao et al., 1996). In these models, sand movement occurs when u_* exceeds a threshold (Shao and Lu, 2000). The u_* is estimated above the roughness "canopy" which includes all roughness elements on the land surface from vegetation to the soil surface (Webb et al., 2020; Ziegler et al., 2020). Field measurements of u_* are typically estimated indirectly from the wind velocity profile (Marticorena et al., 2006; Ziegler et al., 2020), or directly using the eddy covariance method (Dupont et al., 2018). More recently, ultrasonic anemometers have provided the ability to directly measure u_* at a given height (Zhang et al., 2022). Measured in these ways, u_* depends on roughness conditions in the direction of wind movement and may not represent the whole landscape (Chappell et al., 2010; Ziegler et al., 2020). Setting up instruments at multiple locations to accurately estimate

78 the variability of u_* across a landscape is labor-intensive and expensive, and is therefore
79 difficult to achieve. The u_* used in traditional sediment transport and dust emission models at
80 regional scales is usually determined based on the law of the wall using the aerodynamic
81 roughness length (z_0) that is obtained from the roughness density (Darmenova et al., 2009; Xi
82 and Sokolik, 2015; Foroutan et al., 2017). The performance of the model is sensitive to the
83 estimation of $u*$ throughout a region (Pi et al., 2014).

84 The u_* must be partitioned between that extracted by the roughness elements necessary for
85 modelling sediment transport and dust emission (Raupach et al., 1993). It is the momentum
86 which reaches the soil surface (u_{s*}) which drives sediment transport (Webb et al., 2020).
87 Traditional estimates of u_{s*} typically rely on existing drag partition *R*, with parameters that do
88 not adequately represent momentum distribution when applied to regions (Webb et al., 2020).
89 The accurate values $R(z_0, z_{0s})$ are unknown for every pixel and every time step that
90 contributes to sediment transport. The z_0 and z_{0s} values required for these drag partition
91 schemes are not available for all locations, so they are typically set as static values over time
92 and fixed in space to represent the condition of bare soil surfaces. These weaknesses lead to
93 the over-estimation of sediment transport in exemplar traditional models (Chappell et al.,
94 2023b). Chappell and Webb (2016) developed a method for estimating directly u_*/U_h and
95 u_{s*}/U_h over area by using normalised shadow (1-albedo) to represent aerodynamic sheltering.
96 Albedo-based u_*/U_h and u_{s*}/U_h are integrated estimates of landscape surface characteristics
97 and are omni-directional. Combined with wind velocity from meteorological stations at a
98 height of 10 m (U_h), this albedo-based approach partitions shear stress to estimate u_* and u_{s*}
99 at each pixel, enabling the spatio-temporal variation in aerodynamic roughness on a regional
100 or global scale (Chappell et al., 2023a). Ziegler et al. (2020) demonstrated the scale invariance
101 of this approach at the field (plot) scale. This scale invariance has been assumed to hold over

large areas when the albedo-based approach has been applied to dust emission studies in North America (Hennen et al., 2022; 2023) and globally (Chappell et al., 2023a). Considering the existence of multiple, very different, roughness element types, such as plants and gravel, and different spatial combinations (density variation, non-homogeneous spatial distribution) in arid and semi-arid landscapes, it is necessary to further evaluate the applicability of this new approach based on albedo across a representative range of cover types.

Our overall aim was to evaluate albedo-based wind friction velocity from satellite remote sensing and ground-based measurements. Field sites were established along an 1800-km transect across a range of cover types in the Inner Mongolia Autonomous Region of China, an area that is well-known for sediment transport and dust emission. Our specific objectives were to: (1) compare ultrasonic anemometer measurements of u_* and wind speed measurements at a given height (U_h) with albedo-based estimates of u_*/U_h; (2) use field measurements of wide-angle albedo and narrow-angle reflectance to calculate u_*/U_h and compare this value with satellite albedo estimates of u_*/U_h using the albedo-based approach; and (3) quantify the spatial patterns of u_*, u_{S*} and sediment transport on the Inner Mongolia Plateau.

2 Materials and methods

2.1 Study area

The study area is located in the Inner Mongolia Autonomous Region (37°24′N to 53°23′N, 97°12′E to 126°04′E) of the wind erosion prone region of northern China (Fig. 1). The region covers an area of approximately 1.18×10^6 km^2 on the Mongolia Plateau. The landform of the region is dominated by plateaus, with a mosaic of plains and hills, most of which are at elevations above 1000 m above sea level. The regional climate is primarily temperate

monsoonal and continental, with a gradual transition from a semi-humid zone in the east to semi-arid and arid zones in the west. The average annual temperature ranges from 3°C to 6°C, decreasing from south to north. The annual precipitation decreases from 550 mm in the northeast to 50 mm in the southwest, with rainfall mainly concentrated in July to September (Zhang et al., 2018). Northwest and west winds prevail in the region, with an annual average wind velocity of 2.7 to 3.1 m s^{-1}, with maximum wind speeds exceeding 17 m s^{-1} during the windy period from March to May (Zhang et al., 2018). The soils include Phaeozems, Cambisols, Chernozems, Kastanozems, and Arenosols (IUSS Working Group WRB, 2015). As a result of the region's temperature and precipitation gradients, the cover type gradually changes from northeast to southwest, from forest, meadow grassland, and typical grassland in the areas with the greatest precipitation to desert grassland, open shrubland, deserts, and gobis (gravel surfaces) in drier areas, of which grassland landscapes account for 40.9% of the total area (Zhang et al., 2018). The fractional vegetation cover decreases from around 90% in the east to around 10% in the west, with common herbaceous types such as *Leymus chinensis*, *Stipa baicalensis*, *Stipa grandis*, *Stipa krylovii*, *Stipa breviflora*, *Cleistogenes songorica*, and *Allium mongolicum*, and shrubs including *Caragana korshinskii*, *Reaumuria songarica*, *Zygophyllum xanthoxylum*, and *Oxytropis aciphylla*. The westernmost part of the study area comprises gravel-covered gobi surfaces, with the fractional gravel cover ranging from 31.5% to 84.6% (Qian et al., 2014).

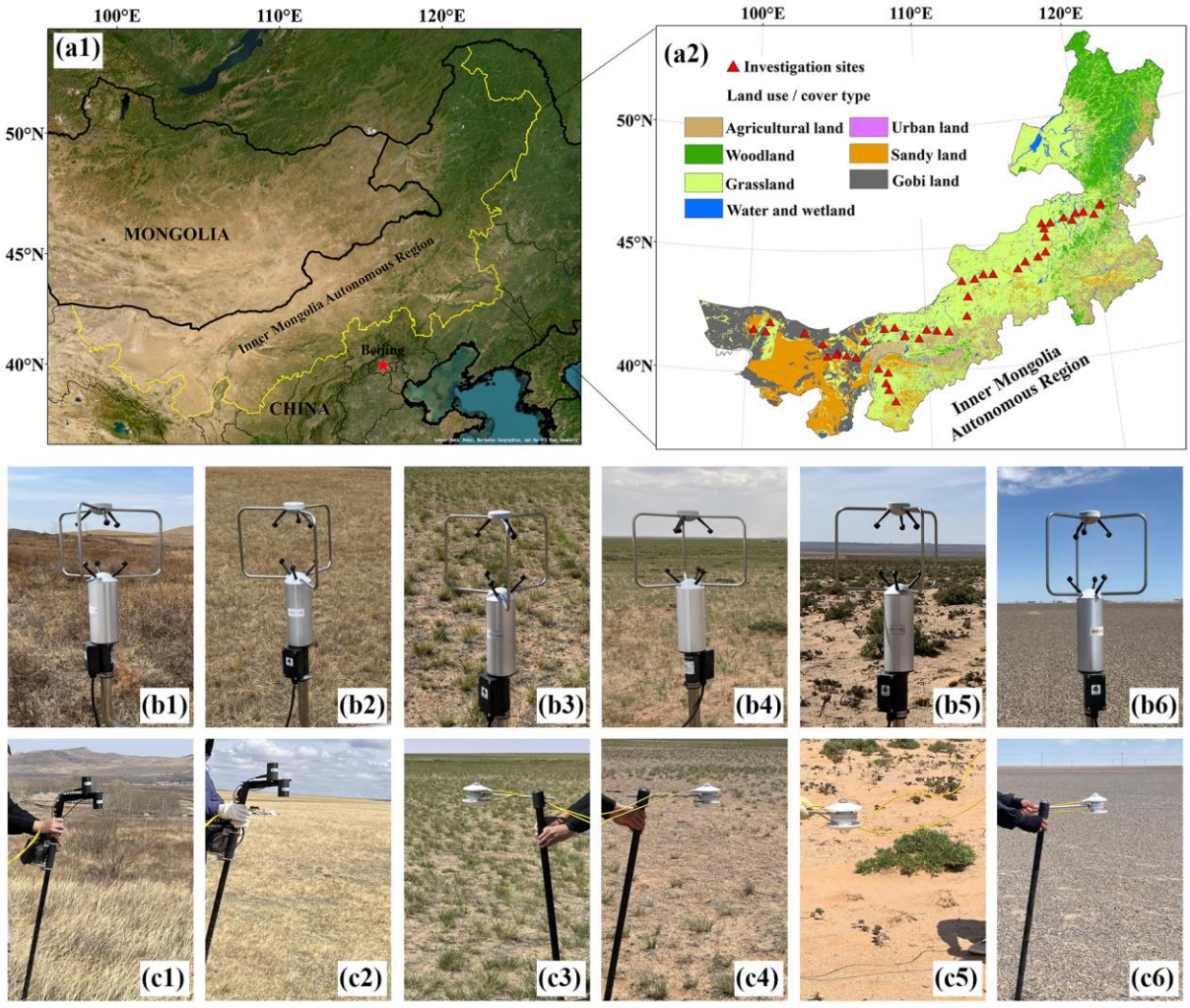

Fig. 1. (a1) Location of the study area in the Inner Mongolia Autonomous region. (a2) Distribution of cover types and the locations of the sample sites. Photographs taken at the different cover types to show (b1 to b6) the three-dimensional ultrasonic anemometers, (c1, c2) reflectance measurements, and (c3 to c6) albedo measurements.

2.2 Field sites

In April to June 2022, we made measurements at 48 sites with level and open roughness "canopy" along an 1800 km transect from the northeast to the southwest on the Inner Mongolia Plateau, with sites chosen to represent the diversity of land cover types in the region. We visited only cover types (grassland, shrubland, gobi) where sediment transport was

154 expected to occur. Each of these cover types was sub-divided for measurements, in to
155 different cover levels (Table 1). Grassland sites (27 sites) had three levels of vegetation cover:
156 meadow grassland (2 sites), typical grassland (11 sites), and desert grassland (14 sites).
157 Shrubland sites (14 sites) were divided between so-called “artificial” shrubland (3 sites) and
158 open shrubland (11 sites). The final cover type was gobi land (7 sites), which had negligible
159 vegetation cover. We investigated the fractional cover and height of the vegetation and gravel
160 by establishing three to five sampling plots at each site, separated by at least 100 m, and used
161 the average of the measurements from the three to five plots to represent each site. The
162 fractional cover and average height of the vegetation and gravel for different cover types are
163 shown in Table 1 as background information.

164 Table 1. Summary of the land cover type sample characteristics.

Land Cover type	Number of sites	Fractional vegetation cover	Fractional gravel cover	Mean height of vegetation (cm)	Mean height of gravel (cm)
Meadow grassland	2	0.90	0	51.64	—
Typical grassland	11	0.60±0.16	0	14.33±6.10	—
Desert grassland	14	0.26±0.09	0.11±0.08	8.05±2.46	0.48±0.23
Artificial shrubland	3	0.46±0.28	0.03±0.05	66.14±32.35	0.10±0.17
Open shrubland	11	0.14±0.04	0.14±0.16	41.11±39.25	0.41±0.39
Gobi land	7	0.02±0.01	0.56±0.17	18.19±11.99	1.12±0.18

165 Each site represented different roughness element types, sizes, spatial configurations, and
166 density characteristics (Table 1; Fig. 2). The grassland roughness elements were mainly
167 perennial bunch and rhizome grasses with relatively homogeneous distributions. The artificial
168 shrubland was dominated by *Caragana korshinskii*, which was distributed in strips
169 perpendicular to the prevailing wind direction. Open shrubland comprised dry dwarf shrubs
170 and semi-shrubs distributed apparently randomly in the landscape. Gobi land was densely
171 covered by gravel, and had a level and relatively smooth surface.

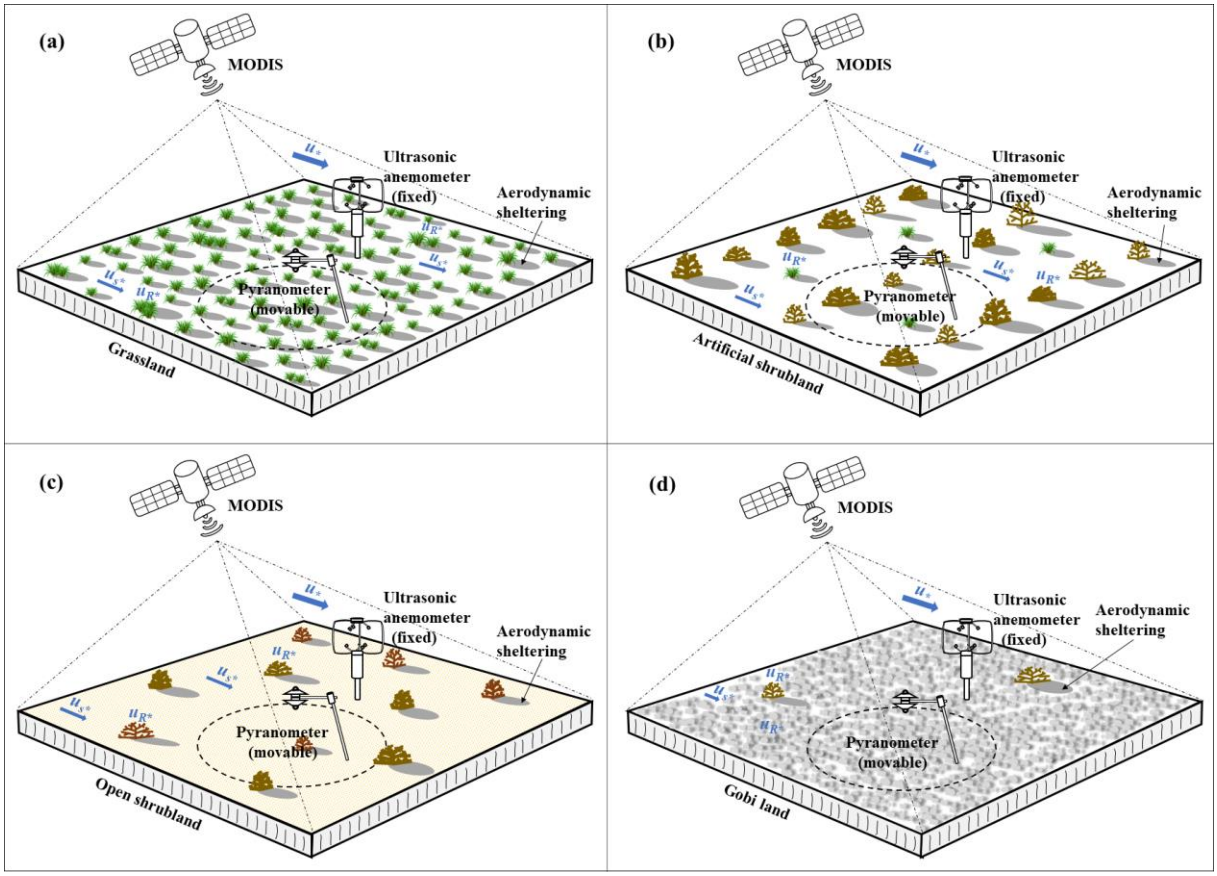

Fig. 2. A schematic representation of the four overall cover types and installations of the three-dimensional ultrasonic anemometers and the pyranometers. Illustrations show typical pixels for the MODIS surface albedo measurements for land cover types with different roughness element types and spatial configurations. The blue arrows indicate the total wind friction velocity (u_*), the roughness element wind friction velocity (u_{R*}) and the soil surface wind friction velocity (u_{S*}) (Adapted from Ziegler et al., 2020).

2.3 Field measurements

The three-dimensional ultrasonic anemometer is a traditional instrument for measuring wind friction velocity in the field, is based on a fast response to wind and turbulence (van Boxel et al., 2004). As a result, the local wind friction velocity can be obtained directly from the correlations between horizontal and vertical pulses of wind velocity (Dupont et al., 2018). At

each site, we measured the wind speed, direction, and wind friction velocity (u_*) using a three-dimensional ultrasonic anemometer (model 81000, R.M. Young, Traverse City, MI, USA). The anemometer was mounted on a post typically at 1 m above the ground. Some shrubland sites required measurements at 1 m to 1.6 m above the ground. At each site, the ultrasonic anemometer was positioned at a single level and in an open location to allow continuous collection of wind speed and direction information. Data was recorded by a datalogger (CR1000, Campbell Scientific, Logan, UT, USA) for between 4 and 7 hours daily (between 10 am and 5 pm) using a recording frequency of 5 Hz.

The land surface albedo measurements were made using two pyranometers (CMP3, Kipp and Zonen, Delft, The Netherlands) in the optical range (300 to 2800 nm) for viewing angles between 0 and 180°; one recorded the incoming radiation and the other recorded the outgoing radiation (after absorption and reflectance). The land surface reflectance (400 to 1100 nm) was obtained by using a two-radiometer combination (a two-channel sensor, SKYE Instruments Ltd, Llandrindod Wells, Wales, UK) that combined the SKR 1840D radiometer for incident light measurements and the SKR 1840ND radiometer for reflected light measurements with a narrow field of view (25°). The pyranometers were positioned at 1 m above the soil surface at most sites (but at 1.5 m at some shrubland sites) and the combination radiometer was placed at 1.5 m above the soil surface at all sites. These instruments were attached to separate hand-held poles that allowed them to be moved to a new position (Fig. 1c). Measurements of albedo and reflectance were made between 11:30 am and 1:30 pm. At each site, the poles were moved to between 8 and 10 locations (at approximately 50-m intervals) in a circle (with a radius of approximately 70 m) around the ultrasonic anemometer. The mean of the measurements from all locations (within a given site) were used as the site's albedo and reflectance.

2.4 Data processing and analysis

2.4.1 Calculation of u_*/U_h separately from albedo field measurements and satellite observations

The albedo-based model developed by Chappell and Webb (2016) uses the normalized and rescaled surface shadow (ω_{ns}) to predict the coupled properties of wind friction velocity normalized by the wind speed (u_*/U_h) and soil surface wind friction velocity normalized by the wind speed (u_{s*}/U_h) (*RMSE* = 0.0027). In those coupled parameters, the influence of wind speed is removed:

$$\frac{u_*}{U_h} = 0.0497\left(1 - \exp\frac{-{\omega_{ns}}^{1.326}}{0.0027}\right) + 0.038 \quad (1)$$

$$\frac{u_{s*}}{U_h} = 0.0311\left(\exp\frac{-{\omega_{ns}}^{1.131}}{0.016}\right) + 0.007 \quad (2)$$

The u_* and u_{s*} was retrieved by multiplying those coupled properties u_*/U_h and u_{s*}/U_h by measured wind speed at a given height of 10 m (U_h) respectively (see Section 2.4.2; Eq. 11).

The ω_{ns} was produced in two different methods. Albedo was retrieved from MODIS data (MODIS/006/MCD43A1) using the data catalogue of the Google Earth Engine. These data were extracted for the study site locations at a spatial resolution of 500 m × 500 m and a daily temporal resolution. Theoretically and in practice, the roughness element structural information should not vary with changes in the wavelength band (Chappell et al., 2018), so we calculated ω_{ns} using MODIS Band 1 (620 to 670 nm):

$$\omega_{ns} = \frac{(a-b)(\omega_n(\theta)-\omega_n(\theta)_{max}}{(\omega_n(\theta)_{min}-\omega_n(\theta)_{max})} + b \quad (3)$$

where a = 0.0001, b = 0.1, $\omega_{n.min}$ = 0, and $\omega_{n.max}$ = 35. Following the method of Chappell et

al. (2018), we used the MODIS isotropic parameter f_{iso} to remove spectral effects due to soil properties such as the moisture content, mineral composition, and soil organic carbon content to calculate the normalized surface shadow ω_n:

$$\omega_n = \frac{1-\omega_{dir}(\theta,v)}{f_{iso}(v)} = \frac{1-\omega_{dir}(0°)}{f_{iso}} \quad (4)$$

where $\omega_{dir}(\theta, v)$ is the albedo at a given zenith angle (θ = 0°), and f_{iso} is an isotropically weighted parameter from the MODIS BRDF model that represents the spectral contribution from the surface.

For data measured in the field with the pyranometer, we calculated ω_{ns} according to the following equation:

$$\omega_{ns} = \frac{(a-b)(\omega_n-\omega_{n.max})}{(\omega_{n.min}-\omega_{n.max})} + b \quad (5)$$

where the calibration parameters are a = 0.0001 and b = 0.1; the minimum rescaling value is $\omega_{n.min}$ = 0; and the maximum rescaling value is $\omega_{n.max}$ = 35, where ω_n is the normalised surface shadow, and Following the method of Ziegler et al. (2020), we used the reflectance to normalize the shadow values and remove the effect of soil properties, as follows:

$$\omega_n = \frac{1-\omega}{R} \quad (6)$$

where ω and R are the albedo and reflectance, respectively, measured in the field at midday. The estimates and field measurements of reflectance had different spectral ranges and representative areas. We corrected field-measured reflectance values with MODIS NBAR values (the at-nadir BRDF-adjusted reflectance) for the pixel that included a given site (Fig. 3) with the values converted from narrowband to broadband using the following equation

(Liang, 2000):

$$\alpha = 0.160\alpha_1 + 0.291\alpha_2 + 0.243\alpha_3 + 0.116\alpha_4 + 0.112\alpha_5 + 0.081\alpha_7 - 0.0015 \quad (7)$$

where α represents the broadband (250 to 2500 nm) value for MODIS NBAR and α_1 to α_7 represent the corresponding narrow bands of MODIS NBAR.

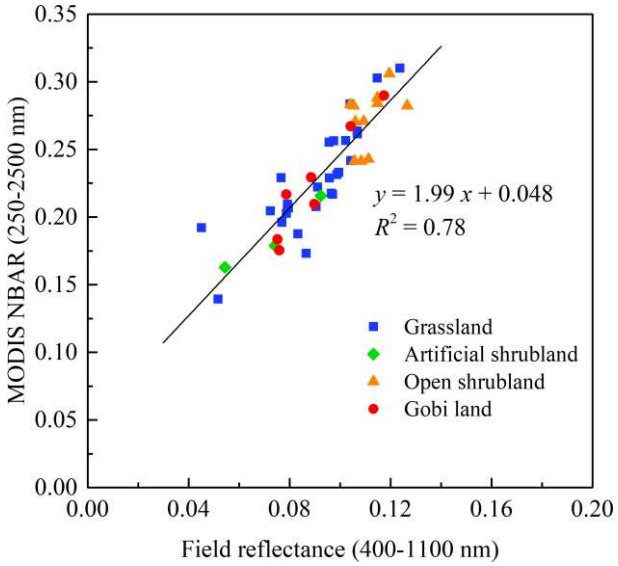

Fig. 3. The relationship between the MODIS NBAR reflectance and the field measurements.

2.4.2 Calculation of u_*/U_h using a three-dimensional ultrasonic anemometer

The wind vectors *u*, *v*, and *w* measured by the three-dimensional ultrasonic anemometer were the components of the three-dimensional *x*–*y*–*z* coordinate system. *u* is the horizontal forward wind speed, *v* is the horizontal lateral wind speed perpendicular to *u*, and *w* is the vertical wind speed perpendicular to both *u* and *v*. We reduced the deviation of the horizontal position and accounted for the direction of the instrument by performing yaw rotation and pitch rotation of the sonic frame of reference (van Boxel et al., 2004).

The average wind speed $\overline{U}$ (m s^{-1}) is the 1-min mean value of the instantaneous wind speed (*U*), and we used this data with coordinate rotation to calculate *U* according to the following

equation:

$$U = \sqrt{u^2 + v^2} \qquad (8)$$

Following the eddy correlation method (Walker, 2005; Zhang et al., 2022), we calculated u_* (m s^{-1}) from the wind velocity pulsation values *u'* and *w'* measured by the ultrasonic anemometer as follows:

$$u_* = \sqrt{\overline{u'w'}} \qquad (9)$$

We calculated the aerodynamic roughness length z_0 (m) for use in extrapolating the wind speed to the standard 10-m height (used in modelled wind fields) consistent with the albedo-based coupling property. We calculated z_0 using the wind profile law:

$$z_0 = (z - d)\exp\left(-k \cdot \frac{U_z}{u*}\right) \qquad (10)$$

where U_z is wind speed at actual height z (in this study, this was typically 1 m but was increased to 1.6 m at some locations) as measured by the ultrasonic anemometer; k is the von Karman-constant (with a value of 0.4); and d is the zero-plane displacement height (m) associated with the roughness element characteristics. We assumed that d was 2/3 of the weighted average height of the roughness elements (Table 1) following the method of Zhang et al. (2012).

To obtain u_*/U_h consistent with the albedo-based approach, the wind speed U_z at the measurement height z of the ultrasonic anemometer calculations, was predicted at the standard height 10 m (U_h) using Eq. 9 and the following equation:

$$U_h = U_z \frac{\log(\frac{10}{z_0})}{\log(\frac{z}{z_0})} \qquad (11)$$

The variation of u_* and U_h over time was calculated using equations (8) and (10), and then the weighted average of u_*/U_h was obtained according to the wind direction for each site (See Supplement S1 for details). In the study region, the wind direction varies around the prevailing wind direction (west to northwest), so we included an adjustment for use in situations where the wind direction influenced the anisotropic aerodynamic roughness.

Considering that the logarithmic wind profile law is not satisfied under very small wind speed conditions, measurements with $\overline{U} < 3$ m s^{-1} were filtered in the above calculations.

2.4.3 Evaluation of u_*/U_h from the ultrasonic and albedo-based methods

We compared estimates of u_*/U_h based on the ultrasonic anemometer and those based on albedo from both ground measurements and MODIS data across the different cover types. The differences between estimates were evaluated using the root-mean-square error (*RMSE*). *RMSE* provides a quantitative indication of the difference between two datasets, and is calculated as follows:

$$RMSE = \sqrt{\frac{\sum_{i=1}^{n}(P_i - O_i)^2}{n - df}} \qquad (12)$$

where P_i and O_i respectively represent the estimated value of the albedo model (either ground-based or from MODIS) and the estimated value of ultrasonic anemometer at location i, and n and df are the number of sampling points and the number of independent variables in the u_*/U_h calculation, respectively. A smaller *RMSE* indicates a smaller difference and greater similarity in u_*/U_h estimated by any two methods.

2.4.4 Seasonal maps of the wind speed, wind friction velocity, and sediment transport

We produced maps of the main properties for each of the main seasons (DJF = December to

February; MAM = March to May; JJA = June to August; and SON = September to November) over the long-term (2001 to 2022) using the Google Earth Engine and the global data available in its catalogue. The long-term seasonal means of u_{s*}/U_h were based on the MODIS albedo data (MODIS/006/MCD43A1) obtained from Google Earth. For comparison, we used the typically static z_0 values assigned to each cover type to produce the u_*/U_h values (See Supplemental Table S1 for lookup tables of the z_0 values for each cover type and the calculated u_*/U_h values). We separately combined the albedo-based u_{s*}/U_h and z_0-based u_*/U_h with the 10-m wind speed data (U_h) from ERA5-Land (Source: European Centre for Medium-Range Weather Forecasts) for the corresponding seasons to produce maps of the spatial distribution of albedo-based u_{s*} and z_0-based u_* for each of the four seasons.

To describe the sheltering effect of surface roughness elements, we calculated the proportion of u_{s*}/U_h based on the MODIS albedo (2001 to 2022) and compared it with the maximum value (u_{s*}/U_h = 0.04) to represent the aerodynamic fraction of erodible soil exposed to wind erosion (*FEW*; i.e., the fraction that is unsheltered) following the method of Chappell et al. (2019) (see Supplement S3).

We produced maps of the mean seasonal (2001 to 2022) sediment transport (g m^{-1} s^{-1}) for the Inner Mongolia Plateau using the traditional modeling approach (Q_T) and the albedo-based approach (Q_A) following the method of Chappell et al. (2023b). Q_T (g m^{-1} s^{-1}) for a given particle size fraction (d), soil moisture content (w), and static aerodynamic roughness length for the landscape (z_0) and the soil (z_{0s}) were calculated as:

$$Q_{\mathrm{T}}(z_0, z_{0\mathrm{s}}, d, w) = \begin{cases} C\frac{\rho_{\mathrm{a}}}{g}u_*^3\left(1-\frac{(u_{*\mathrm{ts}}H/R)^2}{u_*^2}\right)\left(1+\frac{(u_{*\mathrm{ts}}H/R)}{u_*}\right), u_* > u_{*\mathrm{ts}}H/R \\ 0, u_* \le u_{*ts}H/R \end{cases} \quad (13)$$

where ρ_a is the air density (g m^{-3}), g is the acceleration due to gravity (m s^{-2}), C is a

dimensionless fitting parameter, and $u_{*ts}(d)$ is the threshold wind friction velocity (m s^{-1}) adjusted by a function $H(w)$ of the soil moisture content (w; kg^3 kg^{-3}) (Fécan et al, 1999). The calculation of u_* is the same as the calculation for the abovementioned seasonal maps of z_0-based u_*. The u_{s*} is required for sediment flux equations, so the $u_{*ts}H$ is divided by R for the model implementation to account for the drag partition making use of u_* (Webb et al. 2020). Supplemental Eq. 4 describes the calculation of $R(z_0, z_{0s})$.

The Q_A (g m^{-1} s^{-1}) uses the shadow (1 – albedo) to represent the aerodynamic sheltering effect produced by the roughness elements. The Q_A was calculated using the albedo (ω) without R, z_0, or z_{0s}:

$$Q_{\mathrm{A}}(\omega, d, w) = \begin{cases} C\frac{\rho_{\mathrm{a}}}{g}u_{s*}^3\left(1-\frac{(u_{*\mathrm{ts}}H)^2}{u_{\mathrm{s}*}^2}\right)\left(1+\frac{u_{*\mathrm{ts}}H}{u_{\mathrm{s}*}}\right), u_{s*} > u_{*ts}H \\ 0, u_{\mathrm{s}*} \le u_{*\mathrm{ts}}H \end{cases} \quad (14)$$

where the u_{s*} is obtained directly from ω_{ns} and wind speed at a height of 10 m (U_h) (See Section 2.4.1 for details (Eq. 2). The threshold wind friction velocity $u_{*ts}(d)$ and the function $H(w)$ of soil moisture were calculated in the same way by using the same data used for Q_T, and further details of the components can be found in Chappell et al. (2023b).

3 Results

3.1 Differences in aerodynamic properties across land cover types

Table 2 shows the aerodynamic properties of the different cover types. The z_0 values calculated (using Eq.10) based on the ultrasonic anemometer measurements differed among the land cover types. The standard deviation of these values showed large variability within land cover types, especially in the strips of artificial shrubland and the patches of open shrubland, where the roughness elements were non-uniformly distributed (Table 2). There was difference between grassland, shrubland and gobi land cover types. Ultrasonic anemometer-

based u_*/U_h and pyranometer-based and MODIS albedo-based u_*/U_h showed similar differences between land cover types. The soil surface wind friction velocity normalized by wind speed (u_{s*}/U_h) cannot be directly obtained from the ultrasonic anemometer measurements. There were no obvious differences in the broad cover type categories such as all grasslands, all shrublands, and the gobi land, where the albedo-based u_{s*}/U_h was approximately 0.029 to 0.030, but differences were detected among the cover type sub-levels. The values of u_{s*}/U_h based on both pyranometer and MODIS albedo values were largest (i.e., the surface was smoothest) in open shrubland and desert grassland, with values of about 0.031 and 0.030, respectively, indicating that these were the land cover types most susceptible to producing sediment transport. The aerodynamic sheltering effects of gobi land and typical grassland were similar, with pyranometer albedo-based u_{s*}/U_h values of 0.0288±0.0016 and 0.0286±0.0008, respectively. Meadow grassland and artificial shrubland were the roughest surfaces, with pyranometer albedo-based u_{s*}/U_h values of 0.0237 and 0.0271±0.0025.

Table 2. Summary of the aerodynamic properties of the land cover types and their subgroups. Values are the mean and standard deviation of z_0, u_*/U_h and u_{s*}/U_h

Land cover type	Aerodynamic roughness length z_0 (m)	u_*/U_h			u_{s*}/U_h	
		Ultrasonic anemometer	Pyranometer	MODIS	Pyranometer	MODIS
Meadow grassland	0.0533	0.0878	0.0783	0.0723	0.0237	0.0266
Typical grassland	0.0226±0.0042	0.0667±0.0025	0.0671±0.0023	0.0701±0.0031	0.0286±0.0008	0.0275±0.0012
Desert grassland	0.0210±0.0075	0.0640±0.0039	0.0626±0.0019	0.0625±0.0041	0.0303±0.0017	0.0302±0.0006
All grassland	0.0240±0.0115	0.0669±0.0070	0.0658±0.0047	0.0663±0.0054	0.0290±0.0019	0.0289±0.0019
Artificial shrubland	0.0797±0.0337	0.0795±0.0063	0.0707±0.0056	0.0760±0.0032	0.0271±0.0025	0.0249±0.0016
Open shrubland	0.0364±0.0216	0.0707±0.0074	0.0609±0.0018	0.0603±0.0042	0.0308±0.0006	0.0310±0.0014
All shrubland	0.0457±0.0296	0.0725±0.0079	0.0631±0.0050	0.0636±0.0077	0.0300±0.0019	0.0297±0.0030
Gobi land	0.0134±0.0078	0.0578±0.0053	0.0665±0.0045	0.0653±0.0053	0.0288±0.0016	0.0292±0.0019

3.2 Comparison of ultrasonic anemometer measurements with albedo-based estimates

Figure 4 compares the u_*/U_h values across land cover types based on the values retrieved

from albedo-based field pyranometer measurements and satellite remote sensing estimates and ultrasonic anemometer measurements. The pyranometer albedo-based u_*/U_h and MODIS albedo-based u_*/U_h were generally consistent with the ultrasonic anemometer estimates, with *RMSE* values of 0.0082 and 0.0087, respectively. The albedo model performed well for relatively homogeneous grasslands, with u_*/U_h values obtained from the pyranometer albedo that were close to those obtained from the ultrasonic anemometers. For the gobi surface, u_*/U_h values based on the pyranometer albedo and MODIS albedo were slightly larger than those derived from ultrasonic anemometers. For both artificial shrubland and open shrubland surfaces, the u_*/U_h estimates were similar for these methods at most sample sites, but there were obvious deviations in some typically heterogeneous shrub sites, where ultrasonic anemometer measurements at single point cannot represent the actual variation of landscape roughness.

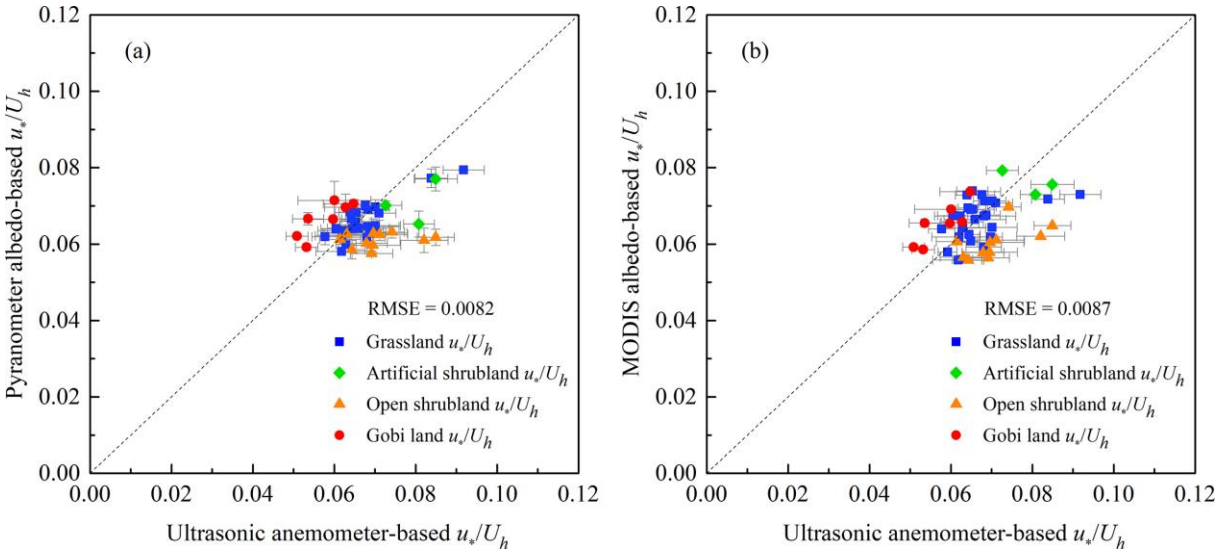

Fig. 4. (a) Pyranometer albedo-based u_*/U_h and (b) MODIS albedo-based u_*/U_h plotted against ultrasonic anemometer-based u_*/U_h.

Figure 5a shows a plot of the independently measured ultrasonic anemometer-based u_*/U_h

against the pyranometer albedo-based ω_{ns}. The figure includes u_*/U_h and u_{s*}/U_h data from Marshall's (1971) wind tunnel experiments and the fitted curves to ω_{ns} (Chappell and Webb, 2016). Independent field measurements of u_*/U_h using ultrasonic anemometers and pyranometer-based ω_{ns} of different land cover types were generally consistent with the distribution of Marshall's (1971) wind tunnel data and close to the fitted curve for u_*/U_h. This demonstrated that the albedo-based model using ω_{ns} can reasonably accurately estimate u_*/U_h and u_{s*}/U_h for different rough surfaces (grass, shrubs, and gravel) in natural environments. The estimates of u_*/U_h and u_{s*}/U_h obtained from field measurements of albedo and MODIS surface albedo scales were strongly consistent, with *RMSE* < 0.004 (Fig. 5b). Although the spectral ranges of albedo and reflectance measured in the field were different from those of the MODIS data, we calibrated the two datasets using a suitable scaling factor ($\omega_{n.max}$ = 35). Therefore, the similarity of these independent measurements from wind tunnels, field measurements, and satellite data confirmed and extended the scale invariance of ω_{ns}-based predictions of u_*/U_h and u_{s*}/U_h (Ziegler et al., 2020).

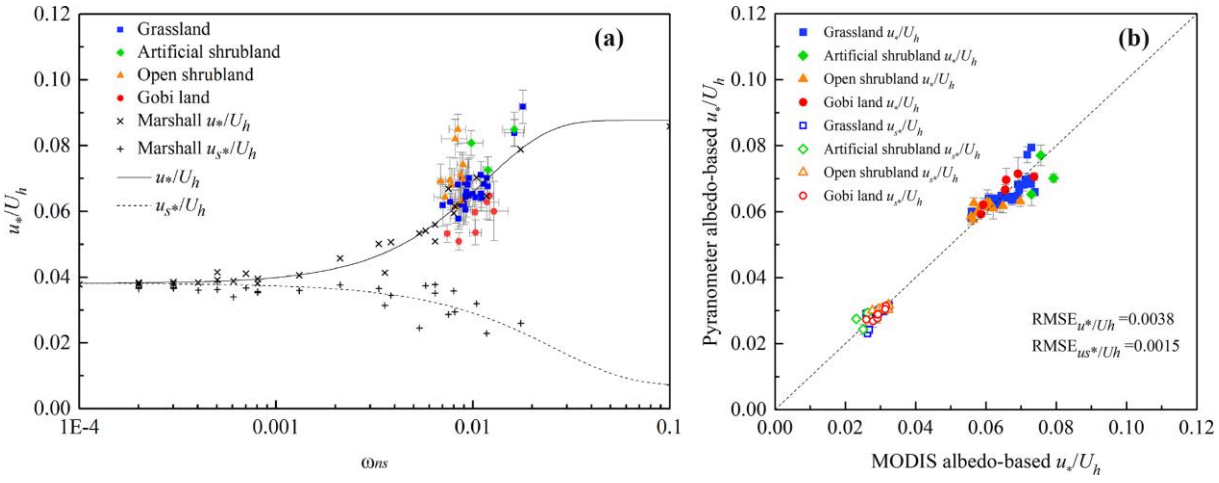

Fig. 5. (a) Ultrasonic anemometer-based u_*/U_h plotted against pyranometer albedo-based normalized shadow ω_{ns}; (b) pyranometer albedo-based u_*/U_h and u_{s*}/U_h plotted against

398 MODIS albedo-based u_*/U_h and u_{s*}/U_h.

399 *3.3 Spatial distribution of wind friction velocity and sediment transport*

400 Wind speeds at a height of 10 m were usually large in MAM (March to May) and small in JJA
401 (June to August) over much of the Inner Mongolia Plateau (Fig. 6). Typically, researchers
402 derive the spatial patterns of u_* at large scales from the MODIS cover types. This method
403 assumes large homogeneous areas with the same z_0 values. In this approach, the u_* values are
404 obtained from a fixed z_0 for each cover type and are considered to be static over time, with
405 seasonal variation solely determined by wind speed and unaffected by seasonal changes in
406 vegetation (Fig. 7a-d). The study sites used in the present study for assigning z_0 values based
407 on land cover types were measured during the non-growing season (Supplemental Table S1),
408 and were unable to represent the spatial and temporal variability over time of surface
409 roughness conditions. The spatial distribution of albedo-based u_{s*} changed daily, although
410 only small variations occurred at the daily-weekly scale. Consequently, the u_{s*} was
411 dynamically determined by the daily variation of the interaction between wind speed and
412 vegetation within each season. There were obvious spatial differences in u_{s*} between seasons
413 on the Inner Mongolia Plateau, showing a gradual decrease from northeast to southwest (Fig.
414 7e-h). In the MAM period, with poor vegetation conditions, a majority of the central and
415 western regions of Inner Mongolia (especially grasslands) demonstrated large values of u_{s*}
416 (smooth land surface); during the JJA period, the u_{s*} values across the entire region decreased
417 as vegetation grew; and as the vegetation wilted and eventually died during the SON
418 (September to November) and DJF (December to February) periods, the u_{s*} values gradually
419 increased.

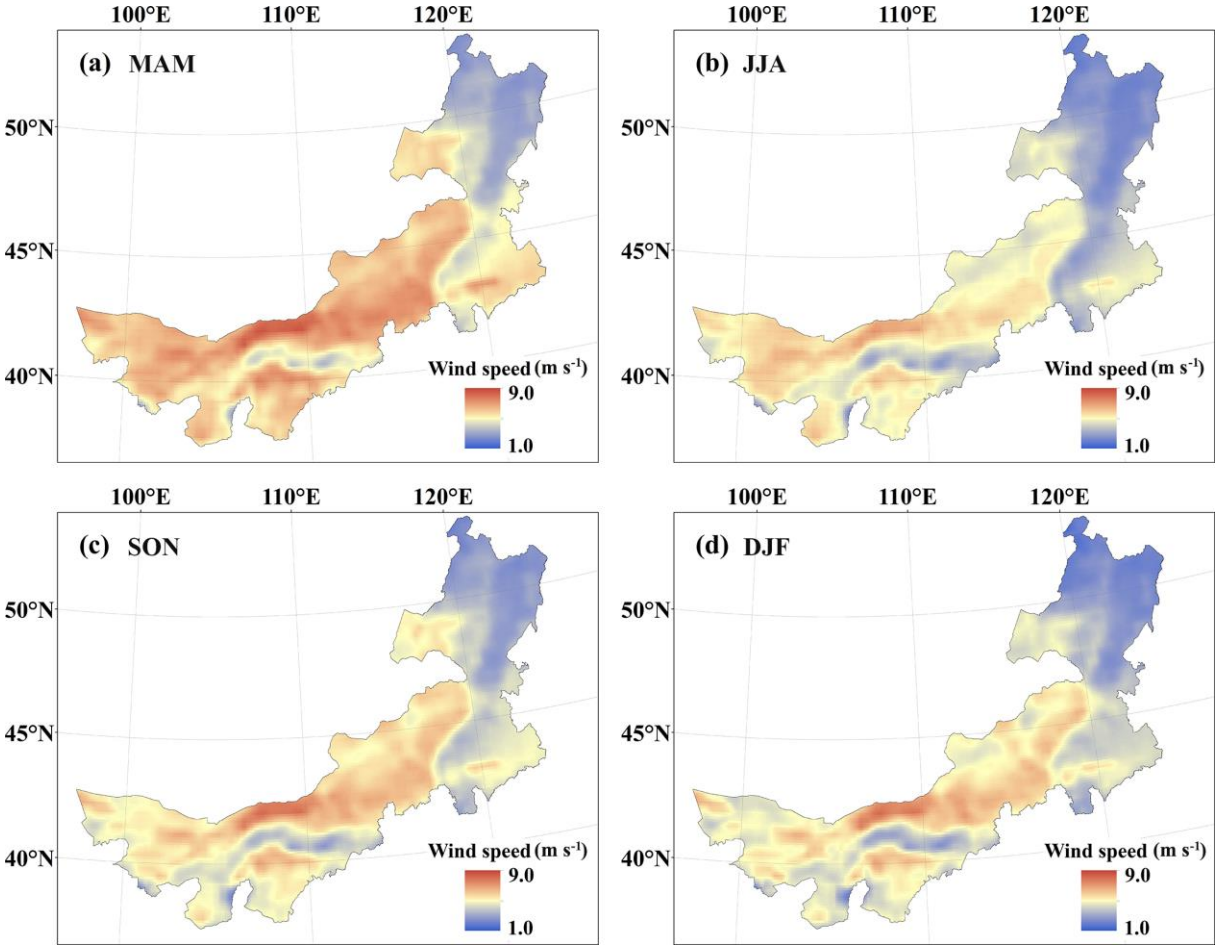

Fig. 6. Average (2001 to 2022) seasonal spatial distribution patterns of wind speed at a 10-m height (m s^{-1}) for (a) MAM (March to May), (b) JJA (June to August), (c) SON (September to November), and (d) DJF (December to February).

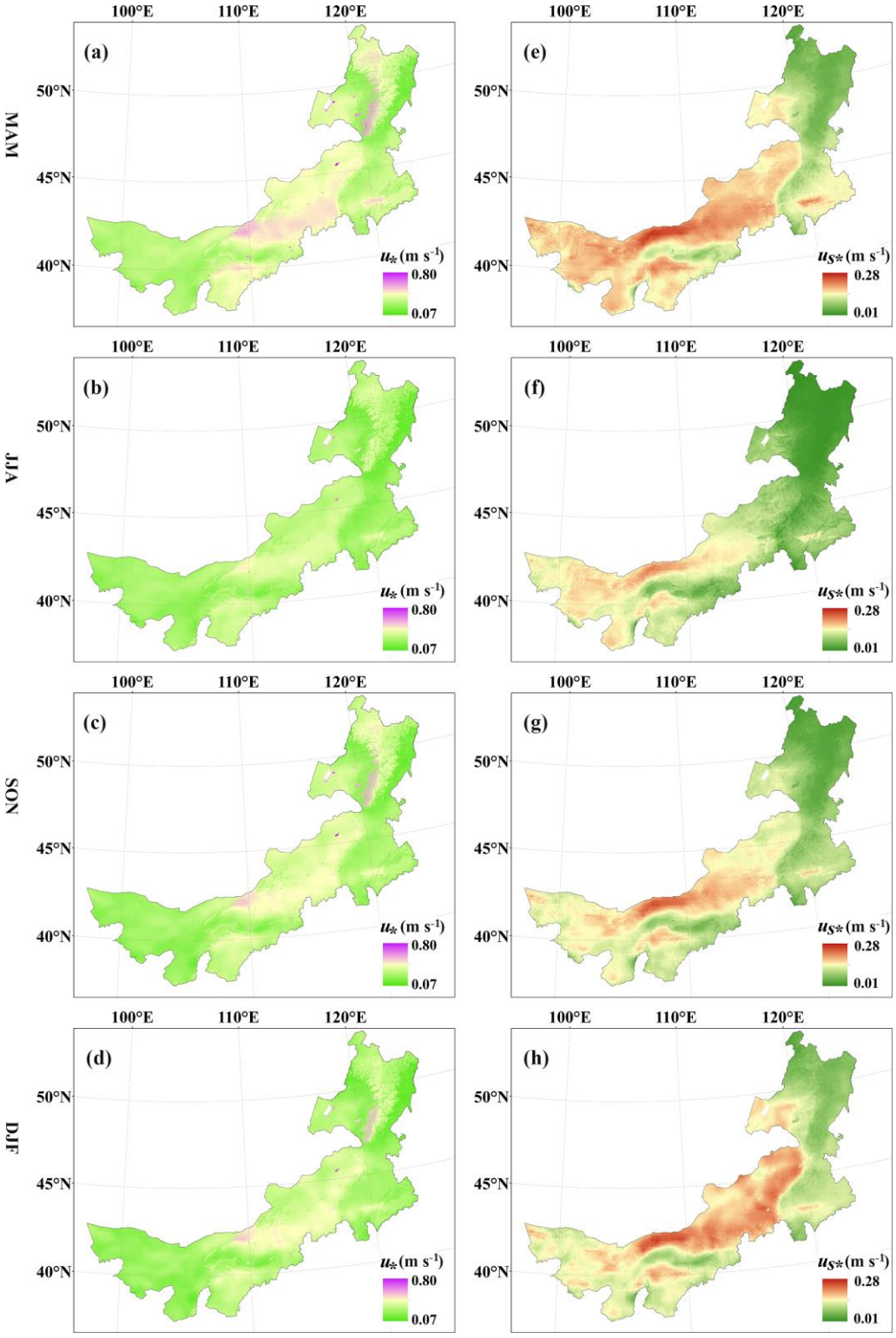

Fig. 7. Average (2001 to 2022) seasonal spatial distribution patterns of (a-d) z_0-based u_* and (e-h) albedo-based u_{s*} for (a,e) MAM (March to May), (b,f) JJA (June to August), (c,g) SON (September to November), and (d,h) DJF (December to February).

We compared the spatial and temporal differences in sediment transport during the four seasons using the exemplar traditional modeling approach (Fig. 8a-d) and the albedo-based approach (Fig. 8e-h). Sediment transport based on the traditional approach generally had a narrower range of values and was larger than the results of the albedo-based approach. Estimates from the traditional model show that most of the western parts of the study area suffered from severe sediment transport. In contrast, the albedo-based approach estimated smaller sediment transport over larger areas. The temporal variation of sediment transport using the traditional model was largely dominated by seasonal difference in wind speed (since $R(z_0, z_{0s})$ was fixed over time). The spatial distribution of *FEW* (Supplemental Figure S1) revealed variation of the unsheltered proportion in response to changes of surface roughness in different seasons. The albedo model combined seasonal differences in wind speed and vegetation, and revealed obvious spatial and temporal variations in sediment transport. During MAM, a period with strong wind speeds and poor sheltering by vegetation, we observed the largest sediment transport. Sediment transport decreased over large areas of the study area as vegetation conditions improved in JJA, but increased in SON. During DJF, the northeastern part of the study area showed large *FEW* values (smooth and bare) influenced by snow cover, but there was no sediment transport due to the frozen ground or snow cover; thus, sediment transport during DJF was much less than in the other seasons.

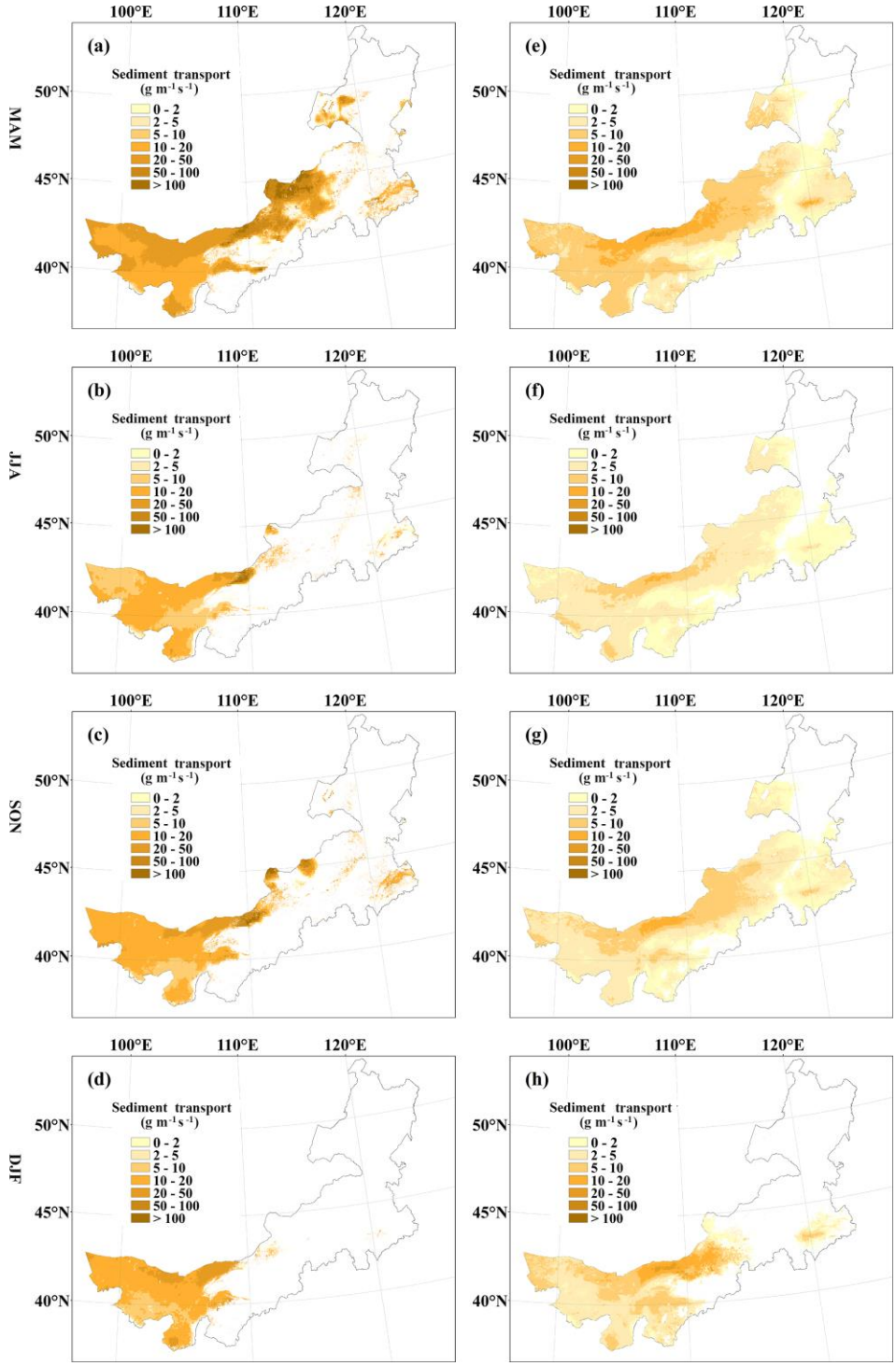

Fig. 8. Spatial distribution of sediment transport (g m^{-1} s^{-1}) from the (a to d) exemplar traditional modeling approach and (e to h) the albedo-based approach for the seasons (a,e) MAM (March to May), (b,f) JJA (June to August), (c,g) SON (September to November), and (d,h) DJF (December to February) over the long-term (2001 to 2022).

4 Discussion

4.1 Applicability of the albedo-based approach across land cover types

Grassland, artificial shrubland, open shrubland, and gobi land are the main land cover types in the arid and semi-arid regions of northern China. In this study, we obtained two independent datasets of wind friction velocity and surface albedo based on *in situ* measurements for cover types with different amounts of roughness. Estimates from both approaches were most consistent in grassland, whereas there were some minor deviations for gobi land, artificial shrubland, and open shrubland (Fig. 4). These error estimates were similar to those of the original calibration (*RMSE* = 0.0027) used to develop the predictive equations for the wind friction velocity (Chappell and Webb, 2016). The vegetation of drylands is characterized by heterogeneous and patchy configurations of roughness elements (Mayaud and Webb, 2017), which makes it difficult to represent that heterogeneity using a single sample point. In contrast, the albedo-based approach developed by Chappell and Webb (2016) integrates the roughness heterogeneity within the sensor's field-of-view range (e.g., from the local scale measured by a pyranometer to the regional scale measured by a satellite) by directly using the surface albedo to provide an integrated estimate of u_*/U_h and more usefully the u_{s*}/U_h which drives sediment transport. In the albedo-based approach, differences and similarities in the number, size, or configuration of surface roughness elements are described by the amount of shadow. In other words, different values of ω_{ns} represent completely different shelter effects, such as large cover meadow grassland and small cover desert grassland surfaces. The approach overcomes the so-called "telephone pole" problem (Okin, 2008) and demonstrates that the same sheltering effects can occur across different land cover types due to their different spatial structures, as in the case of desert grassland and open shrubland.

Based on the pyranometer and MODIS surface albedo, we revealed that meadow grassland, typical grassland, and gobi surfaces had strong sheltering conditions (small u_{s*}/U_h values), whereas desert grassland and open shrubland with low vegetation cover had large u_{s*}/U_h values (Table 2). These results demonstrated that vegetation and gravel (non-erodible) roughness elements extracted similar amounts of momentum from the near-surface airflow, thereby reducing the wind friction velocities at the soil surface (Wiggs et al., 1994; Mayaud et al., 2016; Li et al., 2021). Consequently, the albedo-based approach is effective under the most difficult measurement conditions on heterogeneous surfaces. In short, our field measurements confirm that the albedo-based approach produces appropriate estimates of wind friction velocity for different roughness configurations in different land cover types.

4.2 Confirmed and extended evidence for scale invariance of albedo-based wind friction velocity

Aerodynamic sheltering is a complicated lateral, anisotropic response to the density and configuration of roughness elements (typically vegetation or gravel), and depends on the wind speed. As the size of the area being studied increases, the impact of additional roughness elements is not linearly additive because of the configuration. Consequently, aerodynamic roughness and wind friction velocity don't scale linearly with increasing area (Raupach and Lu, 2004). Consistent with their recommended upscaling solution, the change in the normalized shadow (ω_{ns}) is linearly additive as the pixel area increases, so ω_{ns} increases linearly with increasing scale. After the scaling of ω_{ns} is done, ω_{ns} can be calibrated against wind tunnel measurements of aerodynamic properties to overcome the non-linear scaling problem. The u_*/U_h and u_{s*}/U_h values from both scales (the pyranometer's field-of-view range and the MODIS pixel range) were generally consistent across land cover types (Fig. 5). The differences observed at a few sites may be due to differences in surface roughness

conditions between the two sensors that measured different surfaces in the agropastoral ecotone. By setting the appropriate scaling factor $\omega_{n.max}$ = 35 to calibrate the albedo and reflectance data for different spectral ranges, u_*/U_h and u_{s*}/U_h estimates for a given field-of-view range were broadly consistent with ultrasonic anemometer measurements from the field.

Our findings confirm and extend previous work (Ziegler et al., 2020) across land cover types. Accurate estimation of the areal u_{s*}/U_h is a critical issue that large-scale sediment transport and dust emission prediction studies have been endeavoring to address for more than twenty years since large scale aeolian transport models were first developed (Marticorena and Bergametti, 1995). The values of ω_{ns} can be retrieved and applied at a range of scales, including wind tunnels, pyranometer-based field measurements, and surface albedo data from satellites, thereby enabling the monitoring of spatial and temporal variations in u_{s*}/U_h at local, regional, and even global scales (Ziegler et al., 2020; Hennen et al., 2022, 2023; Chappell et al., 2023a). Our results demonstrate the good performance of albedo-based models across land surfaces and scales in comparison with field measurements at multiple investigation sites across a large area of northern China, thereby providing support for the parameterization of sediment transport and dust emission models.

4.3 Spatio-temporal dynamics in albedo-based sediment transport

We compared the spatio-temporal variation of wind friction velocity and sediment transport using the albedo-based approach and the exemplar traditional model (Fig. 7, 8). We found that the exemplar traditional model based on u_*/U_h considerably overestimated the momentum (u_{s*}/U_h) applied to the soil surface (Webb et al., 2020). Consequently, it overestimated sediment transport relative to the albedo-based approach (calibrated to wind tunnel measurements) and estimated sediment transport in vegetated regions consistent with recent

weaknesses (Chappell et al., 2023b). Furthermore, because the traditional model assumed that z_0 values are fixed for a given cover types and do not change over time (e.g., with seasons, with changing land management, in response to invasive species), the variability in sediment transport in these models was controlled solely by variations in wind speed. In other words, the exemplar traditional model for sediment transport does not account for weakening of the wind caused by the interaction between wind speed and aerodynamic roughness (Chappell et al., 2023b). Changes in crops, grasses, shrubs, and trees from their dormant period to their leaf-on period clearly alter the surface drag partitioning and aerodynamic sheltering, indicating that seasonal changes of vegetation can cause potentially large variations in estimates of the wind erosive forces (Ziegler et al., 2023). Consequently, the exemplar traditional sediment transport model could not represent the spatial and temporal (seasonal) dynamics in sediment transport across land cover types. In contrast, the albedo-based approach using daily MODIS data (here, with 500-m resolution) estimated the soil surface wind friction velocity u_{s*}/U_h directly without the need to calculate aerodynamic roughness length and zero-plane displacement (Chappell and Webb, 2016), which is essential for accurately predicting sediment transport. The approach demonstrated seasonally varying u_{s*}/U_h, leading to attenuation of the wind speed and consequently producing dynamic sediment transport responses (illustrated seasonally; Fig. 7) in different periods that were not controlled solely by variations in wind speed.

In the study area, on the Inner Mongolia Plateau, the quantity of sediment transport using the albedo-based approach was smaller than that estimated by the traditional model approach (Fig. 8). Many previous studies have assessed the wind erosion hazard in this region, and suggested that most of the central and western areas suffer from severe wind erosion hazard (Shi et al., 2007; Zhou et al., 2015, 2016; Wang et al., 2022; Cui et al., 2023). These studies

used the fractional cover of green vegetation observed by satellites as a rough substitute for the aerodynamic sheltering effect of these and other roughness elements. This excludes the "brown" roughness that is common in arid and semi-arid areas, which accounts for non-photosynthetic, dormant, or dead vegetation and non-erodible gravels and is not consistent with the vegetation cover and the resulting sheltering effect of all roughness elements (Chappell et al., 2018, 2023b). Relative to the albedo-based approach (calibrated to wind tunnel measurements), these previous studies underestimated the roughness and overestimated the sediment transport (erosion hazard) on the Inner Mongolia Plateau, where vegetation and gravel roughness elements are widespread in many cover types. A recent study showed that the wind erosion intensity of grasslands on the Inner Mongolia Plateau, with ^{137}Cs-validation, was slight, and had been overestimated by previous wind erosion models (Zhang et al., 2024). Data collected by a number of sediment samplers have demonstrated that the magnitude of sediment transport in the gobi areas and sandy grasslands of northern China was less than 10 g m^{-1} s^{-1} (Sun et al., 2016; Zhang et al., 2021), which is similar to our albedo-based sediment transport quantities (Fig. 8). Therefore, the albedo-based approach sheds light on monitoring of the spatial and temporal dynamics of sediment transport at large scales.

5 Conclusion

In this study, we compared the wind friction velocity between field measurements using an ultrasonic anemometer with the values estimated using the albedo-based approach measured using surface albedo from pyranometer measurements and the MODIS satellite albedo. We compared these approaches in grasslands, artificial shrubland, open shrubland, and gobi land on the Inner Mongolia Plateau. Furthermore, we compared the spatial distributions of seasonal sediment transport between the traditional modeling approach (with fixed z_0 values

for all cover types and static z_0, with no changes over time such as between seasons) and the albedo-based approach.

After calibrating the albedo and reflectance data for different spectral ranges with appropriate scale factors ($\omega_{n.max}$ = 35), we found that the wind friction velocity estimates for a given field-of-view were generally consistent with ultrasonic anemometer measurements in the field. In some areas with non-homogeneous roughness elements, such as open shrubland, single-point measurements based on ultrasonic anemometer may lead to biases in the estimation (indicating the need for representative field sampling). Our study, based on extensive field measurements and evaluations, demonstrated the ability of albedo-based model to mitigate this problem across land cover types and scales.

The albedo-based model let us directly estimate u_{s*}/U_h without the need for separate shear-stress partitioning using aerodynamic roughness length. We used the pyranometer albedo to demonstrate that open shrubland and desert grassland had the largest (aerodynamically smoothest) mean values of u_{s*}/U_h, followed by typical grassland, gobi land, meadow grassland, and artificial shrubland (with the aerodynamically roughest surface). The seasonal variations of u_* obtained from static and fixed z_0 were mainly dominated by seasonal differences in wind speed and were not affected by temporal changes in vegetation cover. In contrast, the spatial and temporal variations of u_{s*} based on albedo resulted from daily changes in the interactions between wind speed and vegetation, which were revealed using seasonal differences.

Sediment flux densities using the traditional modeling approach showed large sediment transport in the western part of the study area in all four seasons, with the greatest transport during the MAM period. In contrast, the albedo-based model showed small sediment transport

over a wide range of the Inner Mongolia Plateau and distinct spatial and temporal variations in sediment transport that were not revealed by the traditional model. Given the established limitations of the exemplar traditional model, the sediment transport estimates of the albedo-based model will enable improved dynamic monitoring of the interactions between wind speed and land surface roughness and will reduce overestimation of regional sediment transport.

Acknowledgments

We thank Mr. Jinguo Liu for his help in the field investigations. This study was supported by the National Natural Science Foundation of China (Grant Nos. U21A2001 and 41630747). AC was supported by NERC (NE/T002263/1, NERCDMP-2634) during the development of this work. We are grateful to Google for use of the Earth Engine and to NASA EOSDIS Land Processes Distributed Active Archive Center (LP DAAC) for providing MODIS data and to ECMWF for providing ERA5-Land data. The manuscript was polished by Mr. Geoff Hart (geoff@geoff-hart.com), a scientific editor from Canada.

Data Availability Statement

The field investigation data can be accessed via this link (https://doi.org/10.6084/m9.figshare.24457309.v1). MODIS data and ERA5-Land data used for regional scale modelling in the main text can be accessed via Google Earth Engine.

Author Contributions

Zhuoli Zhou: Investigation and performing measurements, Methodology, Data analysis, Writing—original draft, Writing—Review & Editing. Chunlai Zhang: Conceptualization, Methodology, Data analysis, Writing—original draft, Writing—Review & Editing. Adrian

Chappell: Conceptualization, Methodology, Data analysis, Writing—original draft, Writing—Review & Editing. Xueyong Zou: Conceptualization. Zhuodong Zhang: Methodology. Xiaofeng Zuo: Investigation and performing measurements. Xiaoyu Zhang: Investigation and performing measurements. Junxiong Zhou: Data processing. Zihao Cao: Data processing.

Competing interests

The authors declare that they have no conflict of interest.

References

Bagnold, R.A. (1941). The Physics of Blown Sand and Desert Dunes, Methuen, London.

Bergametti, G., Marticorena, B., Rajot, J. L., Siour, G., Féron, A., Gaimoz, C., Coman, A., Chatenet, B., Coulibaly, M., Maman, A., Koné, I., Zakou, A. (2020). The respective roles of wind speed and green vegetation in controlling Sahelian dust emission during the wet season. *Geophysical Research Letters*, *47*, e2020GL089761. https://doi.org/10.1029/2020GL089761

Chappell, A., van Pelt, S., Zobeck, T., Dong, Z. (2010). Estimating aerodynamic resistance of rough surfaces using angular reflectance. *Remote Sensing of Environment*, *114* (7), 1462-1470. https://doi.org/10.1016/j.rse.2010.01.025

Chappell, A., Webb, N.P. (2016). Using albedo to reform wind erosion modelling, mapping and monitoring. *Aeolian Research*, *23*, 63-78. https://doi.org/10.1016/j.aeolia.2016.09.006

Chappell, A., Webb, N.P., Guerschman, J.P., Thomas, D.T., Mata, G., Handcock, R.N., Leys, J.F., Butler, H.J. (2018). Improving ground cover monitoring for wind erosion assessment using MODIS BRDF parameters. *Remote Sensing of Environment*, *204*, 756-768. https://doi.org/10.1016/j.rse.2017.09.026

Chappell, A., Webb, N.P., Hennen, M., Schepanski, K., Ciais, P., Balkanski, Y., Zender, C.S., Tegen, I., Zeng, Z., Tong, D., Baker, B., Ekström, M., Baddock, M., Eckardt, F.D., Kandakji, T., Lee, J.A., Nobakht, M., von Holdt, J., Leys, J.F. (2023a). Satellites reveal Earth's seasonally shifting dust emission sources. *Science of The Total Environment*, *883*, 163452. https://doi.org/10.1016/j.scitotenv.2023.163452

Chappell, A., Webb, N.P., Hennen, M., Zender, C.S., Ciais, P., Schepanski, K., Edwards, B.L.,

642 Ziegler, N.P., Balkanski, Y., Tong, D., Leys, J.F., Heidenreich, S., Hynes, R., Fuchs, D.,
643 Zeng, Z., Baddock, M.C., Lee, J.A., Kandakji, T. (2023b). Elucidating hidden and
644 enduring weaknesses in dust emission modelling. *Journal of Geophysical Research:*
645 *Atmospheres*, *128*(17), e2023JD038584. https://doi.org/10.1029/2023JD038584
646 Chappell, A., Webb, N.P., Leys, J.F., Waters, C.M., Orgill, S., Eyres, M.J. (2019). Minimising
647 soil organic carbon erosion by wind is critical for land degradation neutrality.
648 *Environmental Science & Policy*, *93*, 43-52. https://doi.org/10.1016/j.envsci.2018.12.020
649 Cui, L., Shen, Z., Liu, Y., Yu, C., Lu, Q., Zhang, Z., Gao, Y., Nie, T. (2023). Identification of
650 driving forces for windbreak and sand fixation services in semiarid and arid areas: a case
651 of Inner Mongolia, China. *Progress in Physical Geography: Earth and Environment*,
652 *47*(1), 32-49. https://doi.org/10.1177/03091333221105403
653 Darmenova, K., Sokolik, I.N., Shao, Y., Marticorena, B., Bergametti, G. (2009). Development
654 of a physically based dust emission module within the Weather Research and Forecasting
655 (WRF) model: assessment of dust emission parameterizations and input parameters for
656 source regions in Central and East Asia. *Journal of Geophysical Research: Atmospheres*,
657 *114*, D14201. https://doi.org/10.1029/2008JD011236
658 Dupont, S., Rajot, J-L., Labiadh, M., Bergametti, G., Alfaro, S. C., Bouet, C., Fernandes, R.,
659 Khalfallah, B., Lamaud, E., Marticorena, B., Bonnefond, J-M., Chevaillier, S., Garrigou,
660 D., Henry-des-Tureaux, T., Sekrafi, S., Zapf, P. (2018). Aerodynamic parameters over an
661 eroding bare surface: reconciliation of the law of the wall and eddy covariance
662 determinations. *Journal of Geophysical Research: Atmospheres*, *123*, 4490-4508.
663 https://doi.org/10.1029/2017JD027984
664 Fécan, F., Marticorena, B., Bergametti, G. (1999). Parametrization of the increase of the
665 aeolian erosion threshold wind friction velocity due to soil moisture for arid and semi-
666 arid areas. *Annales Geophysicae*, *17*(1), 149-157. https://doi.org/10.1007/s00585-999-
667 0149-7
668 Foroutan, H., Young, J., Napelenok, S., Ran, L., Appel, K.W., Gilliam, R.C., Pleim, J.E.
669 (2017). Development and evaluation of a physics-based windblown dust emission
670 scheme implemented in the CMAQ modeling system. *Journal of Advances in Modeling*
671 *Earth Systems*, *9*, 585-608. https://doi.org/10.1002/2016MS000823
672 Hennen, M., Chappell, A., Edwards, B.L., Faist, A.M., Kandakji, T., Baddock, M.C., Wheeler,
673 B., Tyree, G., Treminio, R., Webb, N.P. (2022). A North American dust emission

climatology (2001-2020) calibrated to dust point sources from satellite observations. *Aeolian Research*, *54*, 100766. https://doi.org/10.1016/j.aeolia.2021.100766

Hennen, M., Chappell, A., Webb, N.P. (2023). Modelled direct causes of dust emission change (2001-2020) in southwestern USA and implications for management. *Aeolian Research*, *60*, 100852. https://doi.org/10.1016/j.aeolia.2022.100852

IUSS Working Group WRB (2015). World Reference Base for Soil Resources 2014. FAO, Rome.

Kok, J.F., Storelvmo, T., Karydis, V.A. Adebiyi, A.A., Mahowald, N.M., Evan, A.T., He, C., Leung, D.M. (2023). Mineral dust aerosol impacts on global climate and climate change. *Nature Reviews Earth & Environment*, *4*, 71-86. https://doi.org/10.1038/s43017-022-00379-5

Lal, R. (2003). Soil erosion and the global carbon budget. *Environment International*, *29*, 437-450. https://doi.org/10.1016/S0160-4120(02)00192-7

Li, H., Zou, X., Zhang, M., Kang, L., Zhang, C., Cheng, H., Wu, X. (2021). A modified Raupach's model applicable for shear-stress partitioning on surfaces covered with dense and flat-shaped gravel roughness elements. *Earth Surface Processes and Landforms*, *46*, 907-920. https://doi.org/10.1002/esp.5052

Liang, S. (2000). Narrowband to broadband conversions of land surface albedo I algorithms. *Remote Sensing of Environment*, *76*, 213-238. https://doi.org/10.1016/S0034-4257(00)00205-4

Marshall, J. K. (1971). Drag measurements in roughness arrays of varying density and distribution. *Agricultural Meteorology*, *8*, 269-292. https://doi.org/10.1016/0002-1571(71)90116-6

Marticorena, B., Bergametti, G. (1995). Modeling the atmospheric dust cycle: 1. Design of a soil-derived dust emission scheme. *Journal of Geophysical Research: Atmospheres*, *100*, 16415-16430. https://doi.org/10.1029/95JD00690

Marticorena, B., Kardous, M., Bergametti, G., Callot, Y., Chazette, P., Khatteli, H., Le Hégarat-Mascle, S., Maillé, M., Rajot, J., Vidal-Madjar, D., Zribi, M. (2006). Surface and aerodynamic roughness in arid and semiarid areas and their relation to radar backscatter coefficient. *Journal of Geophysical Research: Earth Surface*, *111*, F03017. https://doi.org/10.1029/2006JF000462

Mayaud, J.R., Webb, N.P. (2017). Vegetation in drylands: effects on wind flow and aeolian

sediment transport. *Land*, *6*, 64. https://doi.org/10.3390/land6030064

Mayaud, J.R., Wiggs, G.F.S., Bailey, R.M. (2016). Dynamics of skimming flow in the wake of a vegetation patch. *Aeolian Research*, *22*, 141-151. https://doi.org/10.1016/j.aeolia.2016.08.001

Okin, G.S. (2008). A new model of wind erosion in the presence of vegetation. Journal of *Geophysical Research: Earth Surface*, *113*, F02S10. https://doi.org/10.1029/2007JF000758

Pi, H., Sharratt, B. (2017). Evaluation of the RWEQ and SWEEP in simulating soil and PM_{10} loss from a portable wind tunnel. *Soil and Tillage Research*, *170*, 94-103. https://doi.org/10.1016/j.still.2017.03.007

Pi, H., Sharratt, B., Feng, G., Zhang, X. (2014). Comparison of measured and simulated friction velocity and threshold friction velocity using SWEEP. *Soil Science*, *179*, 393-402. DOI: 10.1097/SS.0000000000000082

Qian, G., Dong, Z., Luo, W., Feng, Y., Wu, B., Yang, W. (2014). Gravel morphometric analysis based on digital images of different gobi surfaces in Northwestern China. *Journal of Desert Research*, *34*(3), 625-633 (in Chinese with English abstract).

Raupach, M. R., Lu, H. (2004). Representation of land-surface processes in aeolian transport models. *Environmental Modelling & Software*, *19*(2), 93-112. https://doi.org/10.1016/S1364-8152(03)00113-0

Raupach, M.R., Gillette, D.A., Leys, J.F. (1993). The effect of roughness elements on wind erosion threshold. *Journal of Geophysical Research: Atmospheres*, *98*, 3023-3029. https://doi.org/10.1029/92JD01922

Shao, Y., Lu, H. (2000). A simple expression for wind erosion threshold friction velocity. *Journal of Geophysical Research: Atmospheres*, *105*, 22437-22443. https://doi.org/10.1029/2000JD900304

Shao, Y., Raupach, M.R., Leys, J.F. (1996). A model for predicting aeolian sand drift and dust entrainment on scales from paddock to region. *Australian Journal of Soil Research*, *34*, 309-342. https://doi.org/10.1071/SR9960309

Shi, H., Liu, J., Zhuang, D., Hu, Y. (2007). Using the RBFN model and GIS technique to assess wind erosion hazard of Inner Mongolia, China. *Land Degradation & Development*, *18*, 413-422. https://doi.org/10.1002/ldr.784

Sterk, G., Herrmann, L., Bationo, A. (1996). Wind-blown nutrient transport and soil

productivity changes in southwest Niger. *Land Degradation & Development*, 7, 325-335. https://doi.org/10.1002/(SICI)1099-145X(199612)7:4<325::AID-LDR237>3.0.CO;2-Q

Sun, Y., Hasi, E., Liu, M., Du, H., Guan, C., Tao, B. (2016). Airflow and sediment movement within an inland blowout in Hulun Buir sandy grassland, Inner Mongolia, China. *Aeolian Research*, *22*, 13-22. https://doi.org/10.1016/j.aeolia.2016.05.002

van Boxel, J.H., Sterk, G., Arens, S.M. (2004). Sonic anemometers in aeolian sediment transport research. Geomorphology 59, 131-147. https://doi.org/10.1016/j.geomorph.2003.09.011

Walker, I.J. (2005). Physical and logistical considerations of using ultrasonic anemometers in aeolian sediment transport research. Geomorphology 68, 57-76. https://doi.org/10.1016/j.geomorph.2004.09.031

Wang, Y., Xiao, Y., Xu, J., Xie, G., Qin, K., Liu, J., Niu, Y., Gan, S., Huang, M. (2022). Evaluation of Inner Mongolia wind erosion prevention service based on land use and the RWEQ model. *Journal of Resources and Ecology*, *13*(5), 763-774. DOI: 10.5814/j.issn.1674-764x.2022.05.002

Webb, N.P., Chappell, A., Legrand, S.L., Ziegler, N.P., Edwards, B.L. (2020). A note on the use of drag partition in aeolian transport models. *Aeolian Research*, 42, 100560. https://doi.org/10.1016/j.aeolia.2019.100560

Wiggs, G.F.S., Livingstone, I., Thomas, D. S. G., Bullard, J. E. (1994). Effect of vegetation removal on airflow patterns and dune dynamics in the southwest Kalahari desert. *Land Degradation & Development*, *5*, 13-24. https://doi.org/10.1002/ldr.3400050103

Xi, X., Sokolik, I.N. (2015). Seasonal dynamics of threshold friction velocity and dust emission in Central Asia. *Journal of Geophysical Research: Atmospheres*, 120, 1536-1564. https://doi.org/10.1002/2014JD022471

Zhang, C., Yuan, Y., Zou, X., Wang, H., Li, Q., Wang, Z., Wang, R. (2022). A comparison of the aerodynamic characteristics of four kinds of land surface in wind erosion areas of northern China. *Catena*, *212*, 106112. https://doi.org/10.1016/j.catena.2022.106112

Zhang, H., Fan, J., Cao, W., Harris, W., Li, Y., Chi, W., Wang, S. (2018). Response of wind erosion dynamics to climate change and human activity in Inner Mongolia, China during 1990 to 2015. *Science of The Total Environment*, *639*, 1038-1050. https://doi.org/10.1016/j.scitotenv.2018.05.082

Zhang, Q., Zeng, J., Yao, T. (2012). Interaction of aerodynamic roughness length and

windflow conditions and its parameterization over vegetation surface. *Chinese Science Bulletin*, *57*, 1559-1567. https://doi.org/10.1007/s11434-012-5000-y

Zhang, X., Zhang, C., Zuo, X., Zou, X., Wang, X., Zhao, J., Li, W., Zhou, Z., Zhang, Y. (2024). Extension of the revised wind erosion equation (RWEQ) to calculate grassland wind erosion rates based on the ^{137}Cs tracing technique. *Catena*, *234*, 107544. https://doi.org/10.1016/j.catena.2023.107544

Zhang, Z., Han, L., Pan, K. (2021). Sediment transport characteristics above a gobi surface in northwestern China, and implications for aeolian environments. *Aeolian Research*, *53*, 100745. https://doi.org/10.1016/j.aeolia.2021.100745

Zhou, Y., Guo, B., Wang, S., Tao, H. (2015). An estimation method of soil wind erosion in Inner Mongolia of China based on geographic information system and remote sensing. *Journal of Arid Land*, *7*, 304-317. DOI: 10.1007/s40333-015-0122-0

Zhou, Y., Guo, B., Wang, S., Tao, H., Liu, W., Yang, G., Zhu, J. (2016). Dynamic monitoring of soil wind erosion in Inner Mongolia of China during 1985–2011 based on geographic information system and remote sensing. *Natural Hazards*, *83*, 1-17. https://doi.org/10.1007/s11069-015-1763-1

Ziegler, N. P., Webb, N. P., Chappell, A., LeGrand, S. L. (2020). Scale invariance of albedo-based wind friction velocity. *Journal of Geophysical Research: Atmospheres*, *125*, e2019JD031978. https://doi.org/10.1029/2019JD031978

Ziegler, N. P., Webb, N. P., Gillies, J. A., Edwards, B. L., Nikolich, G., Van Zee, J. W., Cooper, B. F., Browning, B. M., Courtright, E. M., LeGrand, S. L. (2023). Plant phenology drives seasonal changes in shear stress partitioning in a semi-arid rangeland. *Agricultural and Forest Meteorology*, *330*, 109295. https://doi.org/10.1016/j.agrformet.2022.109295

Zou, X., Li, H., Kang, L., Zhang, C., Jia, W., Gao, Y., Zhang, J., Yang, Z., Zhang, M., Xu, J., Cheng, H., Wu, X. (2022). Soil wind erosion rate on rough surfaces: a dynamical model derived from an invariant pattern of the shear-stress probability density function of the soil surface. *Catena*, *219*, 106633. https://doi.org/10.1016/j.catena.2022.106633